

Regional boreal summer intraseasonal oscillation over Indian Ocean and Western Pacific: comparison and predictability study

Sun-Seon Lee¹ · Bin Wang^{1,2}

Received: 20 November 2014 / Accepted: 1 June 2015 / Published online: 7 July 2015
© Springer-Verlag Berlin Heidelberg 2015

Abstract The boreal summer intraseasonal oscillation (BSISO) has two major activity centers, the northern Indian Ocean and tropical Western North Pacific, which dominate the monsoon intraseasonal variability over South Asia and East Asia, respectively. The spatial–temporal structures of BSISO over the Indian Ocean (10°S–30°N, 60°–105°E) (IOISO) and Western Pacific (10°S–30°N, 105°–150°E) (WPISO) are examined by corresponding the leading modes of daily OLR and 850-hPa zonal wind (U850). The IOISO features a northeastward propagation with a 30–45 days energy peak and the first principal component (PC1) has maximum variance in May, while the WPISO propagates northward with a broad spectral peak on 10–60 days and the PC1 has maximum variance in August. Because of the large regional differences, two regional indices, the IOISO index and WPISO index, are defined by their corresponding first two leading PCs. The combined IOISO–WPISO index captures about 30 % (10 %) of U850 (OLR) daily variance over the entire IO–WP region (10°S–30°N, 60°–150°E), which doubles that captured by the Madden–Julian Oscillation (MJO) index (Wheeler and Hendon 2004) and is 50 % higher than that captured by the BSISO index (Lee et al. 2013). The combined index also shows superior performance in representing biweekly and pentad-mean variations in the Asian-Pacific summer monsoon region (north of 10°N). The predictability/prediction

skill and simulated principal modes of two regional BSISO indices are explored by using data derived from the Intra-seasonal Variability Hindcast Experiment project. The major regional modes are reasonably well captured, but the forecasted fractional variances of the leading modes and variability center’s locations exhibit significant deficiencies. The multi-model mean estimate of the predictability is 40–45 days for the IOISO index, whereas 33–37 days for the WPISO index. The less predictable WPISO is likely due to the existence of its significant biweekly component. The multi-model mean prediction skill is significantly higher with large initial amplitude (~20 days for two indices) than that with small initial amplitude (~11 days), suggesting that the prediction for development of BSISO is much more difficult than the prediction for mature BSISO disturbances’ propagation.

Keywords Boreal summer intraseasonal oscillation · Regional ISO · Indian Ocean intraseasonal oscillation · Western Pacific intraseasonal oscillation · Predictability · Prediction skill · Intraseasonal Variability Hindcast Experiment (ISVHE)

1 Introduction

The Indian Ocean (IO) and Western Pacific (WP) are major intraseasonal convective activity centers during boreal summer (e.g. Wang and Rui 1990; Zhu and Wang 1993; Kim et al. 2008) and play a critical role in initiation and propagation of boreal summer intraseasonal oscillation (BSISO) (Kemball-Cook and Wang 2001). Over the IO and WP, the intraseasonal variation of precipitation contributes more than 25 % to the pentad precipitation variance whereas in the central and eastern Pacific the intraseasonal

✉ Bin Wang
wangbin@hawaii.edu

¹ Department of Atmospheric Sciences, International Pacific Research Center and Atmosphere–Ocean Research Center, University of Hawaii at Manoa, Honolulu, HI, USA

² Earth System Modeling Center, Nanjing University of Information Science and Technology, Nanjing 210044, China

variance accounts for only a small percentage (<10 %) (Pegion and Kirtman 2008). In addition, ISO activity in the IO and WP can modulate the formation and development of tropical cyclones (e.g. Liebmann et al. 1994; Maloney and Hartmann 2001; Goswami et al. 2003) and is significantly linked to the extratropical circulation anomalies in the Northern Hemisphere (Moon et al. 2013). These results indicate the importance of understanding the regional BSISO in the IO (IOISO) and WP (WPISO).

Many previous studies have documented the BSISO's features such as spatial–temporal evolutions, periodicity, and linkage with the mean state, focusing on the dominant ISO modes over the entire Asian summer monsoon (ASM) region including both the IO and WP (e.g. Wang and Rui 1990; Zhu and Wang 1993; Kemball-Cook and Wang 2001; Lawrence and Webster 2002; Jiang et al. 2004; Lee et al. 2013, hereafter 'L13'; Suhas et al. 2013; Shukla 2014). Recently, to better monitor and predict BSISO, L13 has proposed the BSISO indices based on the leading empirical orthogonal function (EOF) modes of ISO over the targeted region (also, Suhas et al. 2013; Shukla 2014). These BSISO indices capture more fractional variance over the ASM region than that captured by the real-time multivariate Madden–Julian Oscillation (MJO) index (RMM index, Wheeler and Hendon 2004). However, due to regional differences between the IO and WP, a uniform BSISO index remains deficient in capturing the total daily variance over the ASM region. This motivated the present study in which we attempt to raise the fractional variances represented by the leading EOF modes in order to facilitate monitoring and predicting of ISO.

On intraseasonal time scale, the maximum OLR variance is found over the IO in May and June while it moves to the WP during late summer (Kemball-Cook and Wang 2001; Bellenger and Duvel 2007), indicating different seasonal cycle of ISO over the IO and WP during boreal summer. The IOISO and WPISO are influenced by different mean climatology, thus they may behave differently in addition to their commonality and linkage because the mean climate has strong influence on the behavior of the equatorial waves (Wang and Xie 1996, 1997). Thus far, the IOISO and WPISO have not been systematically compared based on the well-designed metrics. Chou and Hsueh (2010) compared the ISO in the IO and Western North Pacific, but only focused on the northward propagating mechanism.

Meanwhile, the dynamical simulation and prediction of the regional ISO in the state-of-the-art climate models have remained a challenging task (e.g. Waliser et al. 2003; Kim et al. 2008). It was found that the climate models tend to considerably underestimate the large intraseasonal variances over the IO and WP (Waliser et al. 2003; Kim and Kang 2008; Kim et al. 2008). To understand deficiencies in

simulating the ISO phenomena, analysis of models' intrinsic intraseasonal variability (ISV) will be helpful. In addition, study on the predictability of regional BSISO over Indo-Pacific regions has been rare. Using a hybrid atmosphere–ocean coupled model, Fu et al. (2007) showed that the ISO predictability is generally higher over the IO than that over the WP with a maximum of 35 days in the eastern equatorial IO. Better understanding of the regional ISO predictability is important because it can potentially improve the regional ISO prediction skills. Therefore, in the present study, we will use longer hindcast data from multi-models to study the present day prediction skill and predictability based on the regional leading modes of the IOISO and WPISO.

This study aims to compare the observed basic features of the IOISO and WPISO measured by an identical framework. Such a comparison will enhance our understanding of the regional ISO predictability and contribute to find its predictability sources. Furthermore, using current coupled models' experimental data, the principal modes of two regional BSISOs and their predictability and prediction skills will be assessed. Since the models' ISV is closely related to the seasonal monsoon variability and predictability (Waliser et al. 2003), the estimation of predictability and prediction skill of ISO is important for studies of the seasonal mean variability as well as ISO.

The observation data and two experimental datasets of IntraSeasonal Variability Hindcast Experiment (ISVHE) used in this study are described in Sect. 2. In Sect. 3, the observed principal modes of the IOISO and WPISO are identified, and capability of the combined IOISO–WPISO modes to capture total daily and ISO variances over the targeted region is explored. Moreover, the IOISO are contrasted with the WPISO in terms of the periodicity, seasonal distribution of variances, and life cycle. The simulated major modes of two regional BSISOs are described in Sect. 4, and the predictability and prediction skill of the IOISO and WPISO are estimated in Sect. 5. Section 6 summarizes the major findings of this study.

2 Data

2.1 Observation

For the multivariate EOF (MV-EOF) analysis (Wang 1992), the daily zonal wind at 850-hPa (U850) obtained from National Centers for Environmental Prediction (NCEP)/Department of Energy (DOE) Reanalysis II (Kanamitsu et al. 2002) and daily averaged OLR data from NOAA polar orbiting series of satellites (Liebmann and Smith 1996) were used. After removing the slow annual cycle (annual mean and first three harmonics of climatological

annual variation) and the interannual variability (running mean of the preceding 120 days) (L13), the anomalous fields of OLR and U850 were utilized to isolate the major IOISO and WPISO modes.

2.2 Two experimental datasets of ISVHE

The ISVHE project has been accomplished to better understand the physical basis of ISV and determine its predictability. The ISVHE includes two sets of experiments, a long-term free coupled run and a 20-year long hindcast experiment. In the present study, to reveal the features of models' intrinsic ISV, the long-term free run data from four models (ECMWF, JMAC, CMCC, CFS2) were used. The method to obtain OLR and U850 anomalies is same as that adopted in observation. Furthermore, the hindcast data of six coupled models (ABOM1, ABOM2, ECMWF, JMAC, CMCC, CFS2) were analyzed to estimate the predictability and assess current prediction skill of the IOISO and WPISO. Daily anomalies of OLR and U850 were obtained by subtracting model climatology and interannual variability. We used hindcast data for summer from May to October. For further details of the ISVHE project, participating models, and experimental data, the readers are referred to Zhang et al. (2013), Neena et al. (2014b) and Lee et al. (2015).

3 IOISO versus WPISO in observation

3.1 Principal modes of the IOISO and WPISO

Recently, L13 showed the major BSISO modes from the MV-EOF analysis of daily OLR and U850 anomalies during boreal summer (from May to October) over the ASM region (10°S – 40°N , 40° – 160°E), and defined the BSISO index using its leading PCs. If not otherwise specifically defined, hereafter, the BSISO mode and BSISO index refer to the results of L13. To document the evolution of the regional BSISO over the IO and WP, i.e. the IOISO and WPISO, we adopted the same procedure employed by L13 using daily OLR and U850 anomalies but over two separate domains upon the consideration of the ISV center of convective anomaly (Moon et al. 2013) and regional monsoon domains (Yim et al. 2014): the IO domain (10°S – 30°N , 60° – 105°E) and WP domain (10°S – 30°N , 105° – 150°E). In the present study, we mainly focused on the first (EOF1) and second (EOF2) MV-EOF modes.

Figure 1a–c show spatial structures and samples of principal components (PCs) of the first two MV-EOF modes over the IO region. Following L13, the 850-hPa meridional wind was obtained by regressing onto each PC in order to show full horizontal wind field. The spatial structure of

the IOISO EOF1 exhibits a large loading over the equatorial IO (Fig. 1a), and it explains about 13 % of total combined daily variance of OLR and U850 anomalies. This spatial distribution strongly resembles the spatial pattern of the BSISO EOF1 over the corresponding region (Fig. 1g) and the EOF1 of pentad-mean OLR over the South Asian monsoon region (Shukla 2014). The spatial pattern of the IOISO EOF2 is characterized by dominant variability over the Bay of Bengal (Fig. 1b). The overall spatial pattern is similar to that of BSISO EOF2 mode (Fig. 1h), but the positive anomaly center of convection is located west of corresponding center of the BSISO EOF2.

The spatial structures and PC time series of the first two MV-EOF modes over the WP domain are presented in Fig. 1d–f. For both leading modes, the dominant variabilities related to the WPISO are confined to the north of the equator compared with the major modes of the IOISO. The WPISO EOF1 mode, which shows a large loading in the vicinity of northern Philippines (Fig. 1d), is very similar to the spatial distribution of the BSISO EOF1 over the corresponding region. The EOF2 of WPISO exhibits the north–south oriented dipole over the WP (Fig. 1e) and this dipole pattern is also found in the BSISO EOF2 mode over the WP region (Fig. 1h) and the EOF2 mode over South Asia domain (Shukla 2014). The northwest to southeast (NW–SE) slope is one of features of BSISO EOF2 (L13), but the distinct NW–SE tilted structure is not observed in the WPISO EOF2.

The maximum lag-correlation between the IOISO PC1 and WPISO PC1 is 0.41 at 0-day lag. This significant correlation coefficient indicates out-of-phase variations of convection between the IO and WP regions, which is consistent with the BSISO EOF1 mode (Fig. 1g and L13) and the previous findings from the total ISO anomalies (Zhu and Wang 1993). This convection seesaw between the IO and WP is significantly related to the active-break monsoon cycles over those two regions (Zhu and Wang 1993).

3.2 Frictional variance explained by the IOISO and WPISO

Do the regional BSISO indices that are derived from the leading PCs of the IOISO and WPISO better represent daily and ISO variations over the entire ASM region (10°S – 40°N , 40° – 160°E) than the BSISO index? To address this question, we compared the fractional variances of daily OLR and U850 anomalies explained by the first two leading EOF modes of the IOISO, WPISO, BSISO, and MJO. For clarity and simplicity, here we define indices for the IOISO and WPISO by the same way for the MJO (RMM) index of Wheeler and Hendon (2004) and BSISO index of L13, i.e., these indices are all defined by using their corresponding PC1 and PC2. Each of these indices

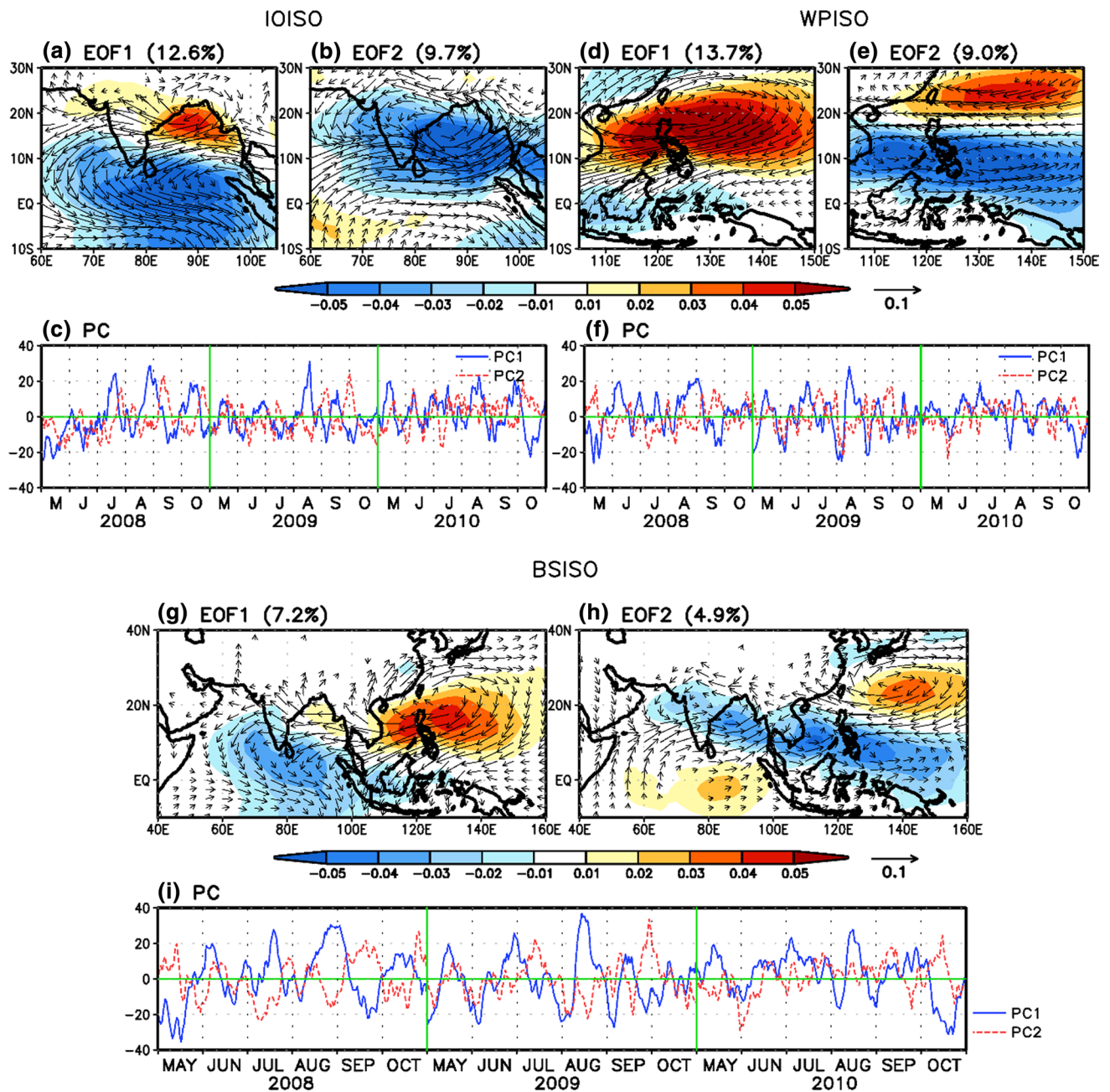


Fig. 1 First two leading MV-EOF modes of daily OLR (shading) and 850-hPa zonal wind (U850) anomalies (MJJASO for the 30 years of 1981–2010). **a, b** Spatial structures and **c** PC time series of the first two leading MV-EOF modes over the IO region (10°S–30°N, 60°–105°E). **d–f** Same as **a–c** except for the WP region

(10°S–30°N, 105°–150°E). **g–i** Same as **a–c** except for the ASM region (10°S–40°N, 40°–160°E). To display the full horizontal wind vector, the associated 850-hPa meridional wind (V850) was obtained by regressing V850 anomaly against each PC

serves as a specific metric to describe the corresponding reconstructed evolution. In particular, to show the fractional variance captured by the IOISO and WPISO together, the combined IOISO–WPISO index is defined by the combination of the IOISO index and WPISO index. The fractional variance explained by the combined IOISO–WPISO index in the region over 10°S–40°N, 40°–160°E indicates that in

the region west of 105°E (inclusive), the two leading PCs of the IOISO are used for calculation of the fractional variance while in the region east of 105°E, the two leading PCs of the WPISO are used.

Figure 2 presents the daily variances of OLR and U850 anomalies for summer (from May to October) explained by the combined IOISO–WPISO index, BSISO index, and

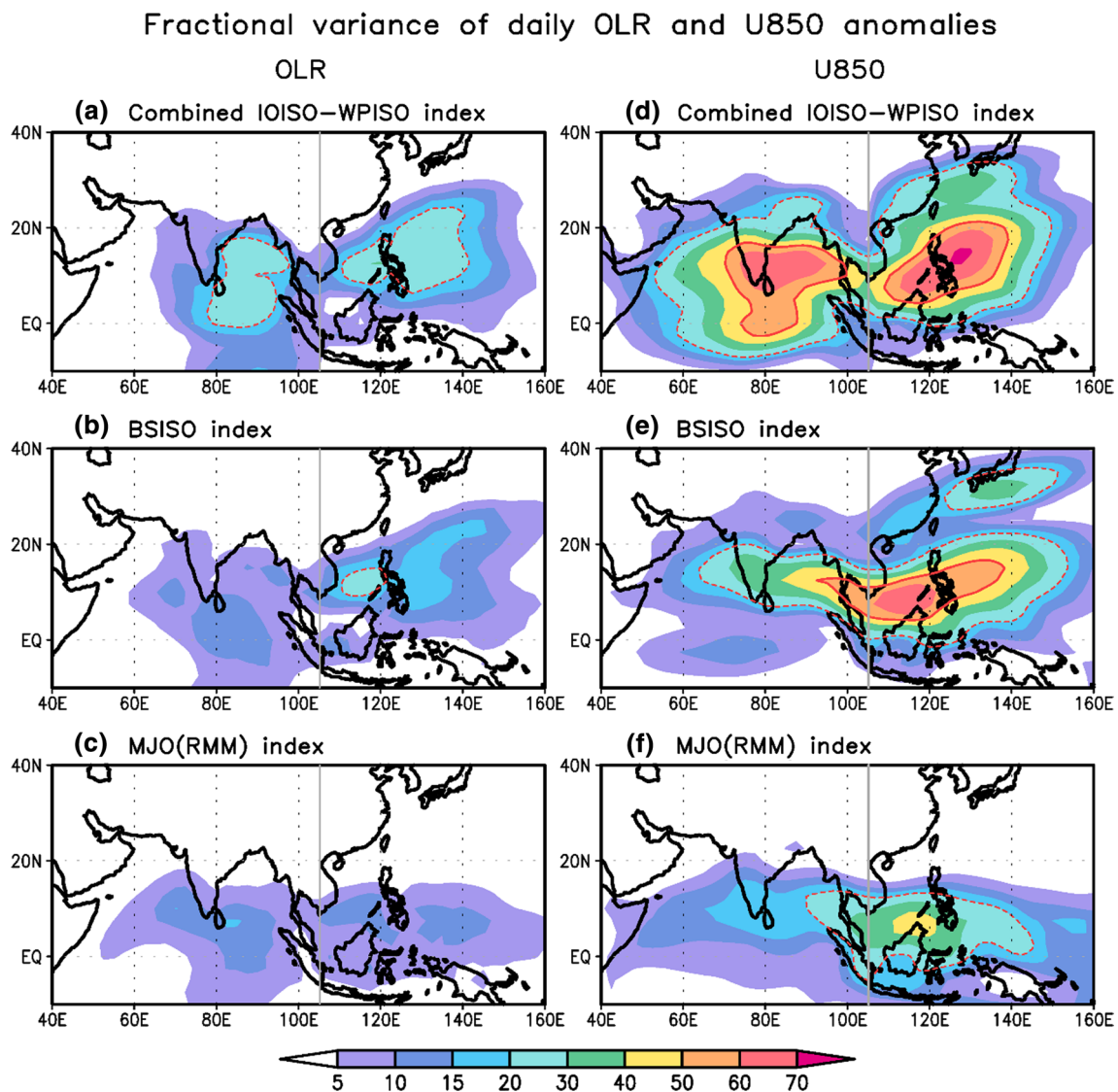


Fig. 2 Spatial distribution of fractional variance of daily OLR (*left panels*) and U850 (*right panels*) anomalies that captured by the **a, d** combined IOISO–WPISO index, **b, e** BSISO index, and **c, f** MJO (RMM) index. The combined IOISO–WPISO index is defined by the combination of the IOISO index and WPISO index. For the daily

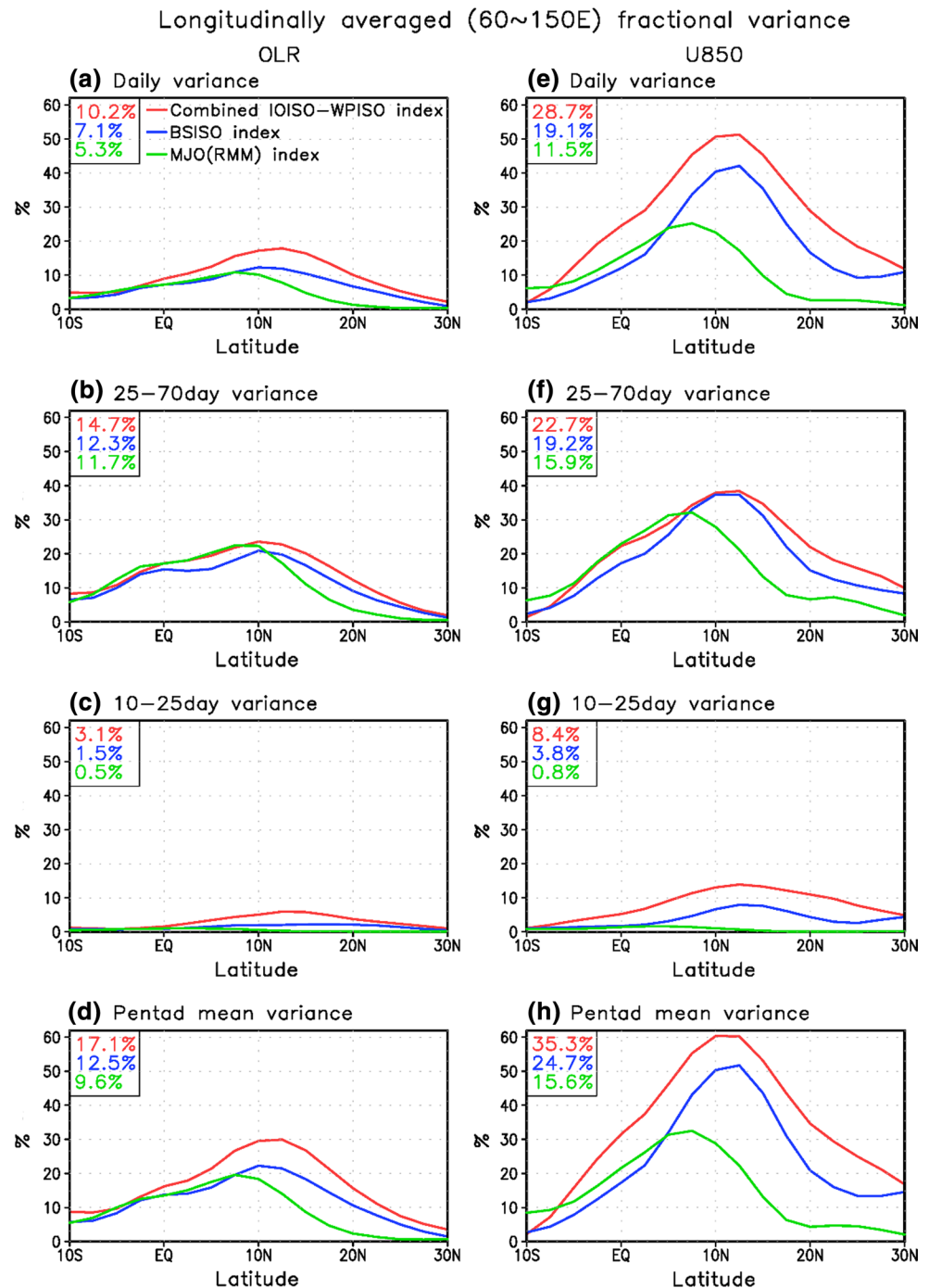
OLR and U850 anomalies, the slow annual cycle (annual mean and first three harmonics of climatological annual variation) and effect of interannual variability were removed. The *red dotted* and *solid contours* represent fractional variance at 20 and 50 %, respectively. The vertical *gray line* indicates 105°E

MJO (RMM) index. It is noted that the combined IOISO–WPISO index captures a considerably larger fraction of daily variances of OLR and U850 in the ASM region compared with the BSISO and MJO (RMM) indices. The combined IOISO–WPISO modes can capture higher than 20 % of OLR daily variance over the eastern IO (Eq–20°N, 80°–100°E) and vicinity of Philippines (10°–20°N, 110°–140°E) (Fig. 2a), but both the BSISO and MJO (RMM) modes account for less than 20 % of OLR daily variance over most of the ASM region. In addition, the combined index can explain higher than 50 % of U850 daily variance over the eastern IO and vicinity of Philippines (Fig. 2d).

Meanwhile, the 10–70 days variance has large portion of daily variance over the IO and WP, particularly higher than 60 % over the Indian Subcontinent and vicinity of Philippines in U850 (figure not shown). This indicates that daily variance of U850 can be better captured by the ISO index compared with that of OLR, therefore the fractional variances of daily U850 accounted for by the three ISO indices are always higher than those of OLR.

Furthermore, the longitudinally averaged (60°–150°E, covering the IO and WP domains) fractional variances explained by the three types of ISO indices were compared as a function of latitude (Fig. 3). Daily, 25–70, 10–25 days,

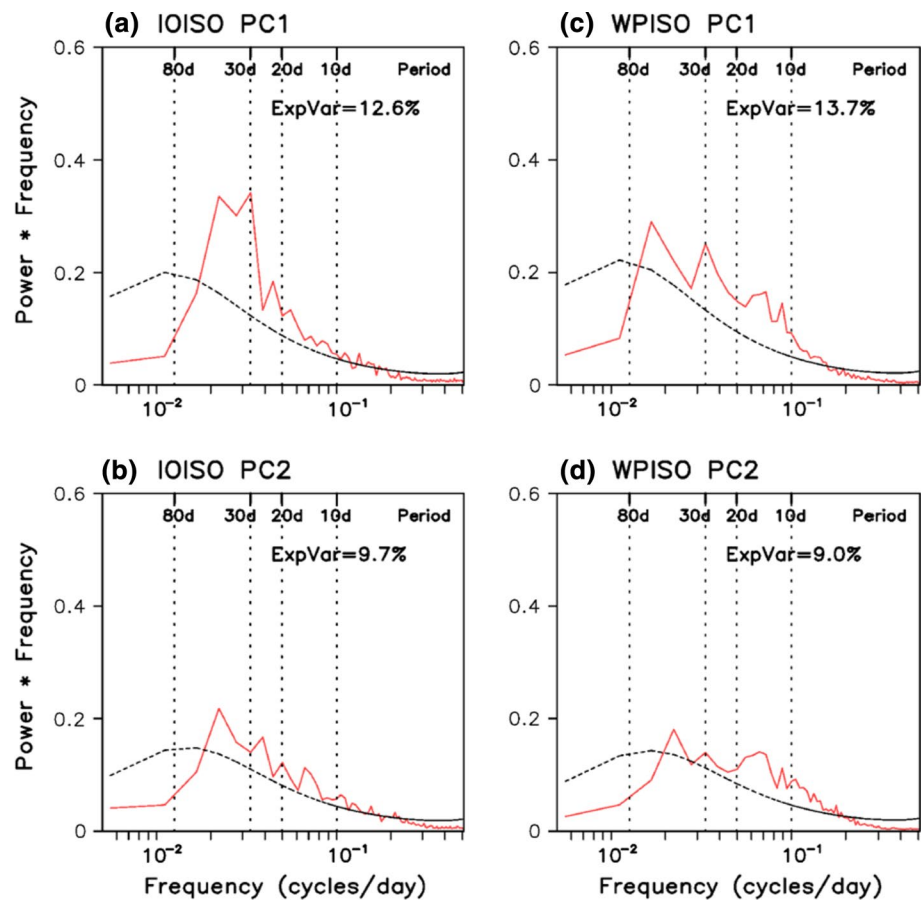
Fig. 3 Longitudinally averaged (60°–150°E) fractional variance of OLR and U850 anomalies explained by the combined IOISO–WPISO index, BSISO index, and MJO (RMM) index. The number at the *top-left corner* indicates the IO–WP area (10°S–30°N, 60°–150°E) averaged fractional variance explained by the combined IOISO–WPISO index (*red*), BSISO index (*blue*), and MJO(RMM) index (*green*)



and pentad-mean variances of OLR and U850 anomalies were analyzed for the detailed comparison. Figure 3 reveals that for all cases the combined IOISO–WPISO index is effective in explaining the variances of OLR and U850 over the IO–WP region. For daily variance (Fig. 3a, e), the combined IOISO–WPISO index captures about 10 % for OLR and 30 % for U850 variance over the IO–WP region (10°S–30°N, 60°–150°E). These values are double that captured by the MJO (RMM) index and are 50 % higher

than that captured by the BSISO index. The fractional variance captured by the MJO (RMM) index is confined to the region from the equator to 10°N, thus main differences of fractional variances explained by the three ISO indices are found north of 10°N. In particular, the combined IOISO–WPISO modes show definite advantages in representing biweekly and pentad-mean variations in the north of 10°N. It can capture about 60 % of pentad-mean variance of U850 at 10°–12.5°N and this value is much greater

Fig. 4 Power spectra of the IOISO PC1 and PC2 (*left panels*) and WPISO PC1 and PC2 (*right panels*). It was separately calculated each year with 184 sample size during MJJASO and then averaged over the 30-years. The plotting format forces the area under the *power curve* in any frequency band to be equal to variance. The total area under *each curve* is scaled to equal the explained variance (Exp Var) by that EOF. The *dashed curve* is the *red-noise spectrum* computed from the lag 1 autocorrelation



than that captured by the MJO index, which is about 30 % in the corresponding latitudes. In addition, the combined regional modes can represent about 10 % of biweekly variation for U850 (Fig. 3g) and this might be due to the multi-time scale variability of the WPISO (Fig. 4c, d, discussed later). Three ISO indices show similar ability to capture the 25–70 days variance. Consequently, results obtained from Figs. 2 and 3 demonstrate an obvious advantage of using regional BSISO indices to represent the total daily and ISO variations over the entire IO–WP region.

3.3 Comparison of the characteristics of regional ISO over the IO and WP

In this subsection, we compared the regional BSISO behaviors between the IO and WP in terms of the periodicity, seasonality, and life cycle with the seasonal preference of its occurrence.

Figure 4 compares the power spectra of the first two PCs for the IOISO and WPISO. The PC1 of the IOISO shows a salient 30–45 days periodicity (Fig. 4a) while the PC1 of the WPISO presents a broad spectral peak ranging from 10 to 60 days (Fig. 4c). This indicates that the dominant ISO modes over the IO and WP have distinguished periodicity.

For ISO over the IO, Krishnamurthy and Shukla (2008) showed two oscillatory modes of 45 and 28 days and these variabilities are related to the Rossby wave (Sengupta et al. 2001), which is emanated from the Sumatra Island and plays an important role in ISO over the IO (Wang and Xie 1997; Kemball-Cook and Wang 2001; Lawrence and Webster 2002). On the other hand, the multi-time scale variability including biweekly, 30 and 60 days is an important feature of the WPISO (Fig. 4c, d). It was found that westward propagating biweekly disturbances are particularly active over the WP (Kikuchi and Wang 2009). The spectra of the WPISO PC3 and PC4 as well as the IOISO PC4 also show biweekly oscillation peaks, but no significant periodicity is observed in the IOISO PC3 (not shown).

Figure 5a presents the seasonal distribution of the four leading PCs' variances of the IOISO and WPISO. For the months of the year outside of May to October, the PC data were obtained by projecting OLR and U850 anomalies onto the corresponding EOF structures (L13). The pronounced difference between the IOISO PC1 and WPISO PC1 is that the maximum variance occurs in May for the IOISO whereas in August for the WPISO, reflecting a seasonal shift of ISO activity from the IO to WP as shown by Kemball-Cook and Wang (2001). Therefore, the BSISO

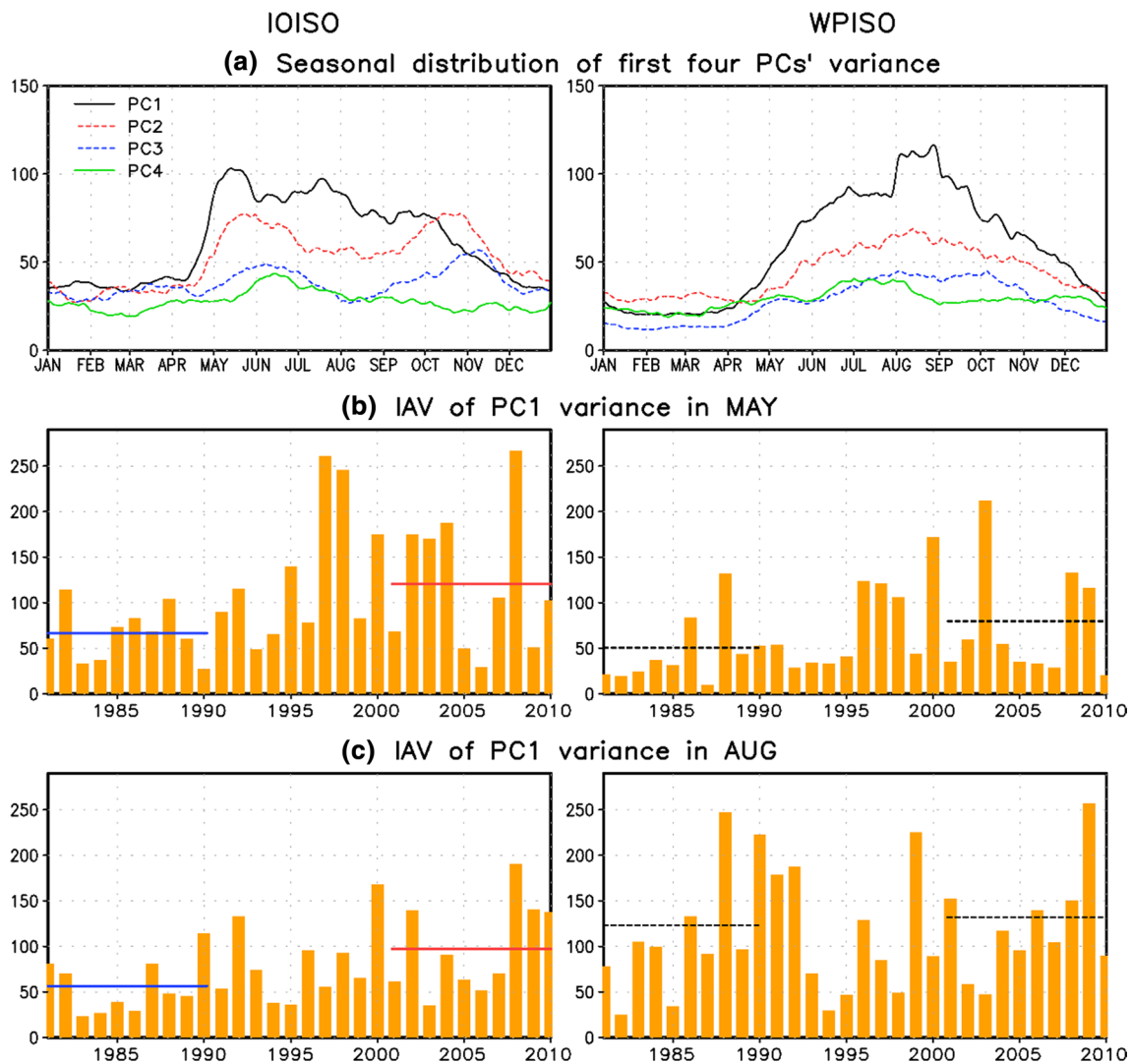


Fig. 5 **a** The seasonal distribution of the first four PCs' variance of the IOISO and WPISO for the 30 years (1981–2010). The interannual variability of PC1 variance of the IOISO and WPISO in **b** May and **c** August. In **(a)**, 31-day running mean was applied. For the interannual variability of the IOISO PC1, the *blue* and *red solid lines* indicate the mean of IOISO PC1 variance for the 10 years of 1981–1990 and 2001–2010, respectively, and the difference of means

between two periods (*blue* and *red lines*) is significant at the 95 % confidence level. For the interannual variability of the WPISO PC1, the *black dotted lines* indicate the mean of WPISO PC1 variance for the 10 years of 1981–1990 and 2001–2010, respectively, and the difference of means between two periods (*two black dotted lines*) is not significant at the 95 % confidence level

PC1 over the entire ASM region shows two peaks in May and August (L13). The PC2 and PC3 of the IOISO have distinct double peaks at May–June and October–November, and these double peaks are reflected in the monthly mean ISV of convection over the IO as documented by Bellenget and Duvel (2007). In contrast, the WPISO PC2 and PC3 exhibit the single peak in August and August–September, respectively.

Furthermore, we examined the interannual variability of each PC's monthly variance to see whether there is an interdecadal trend in the leading PC's variance. It is noted that the mean variances of the IOISO PC1 in May and August

during 2001–2010 are significantly larger than those during 1981–1990 (Fig. 5b, c), indicating that strong anomalous structures associated with the IOISO EOF1 (Fig. 1a) frequently occur in May and August during the 2000s compared with the 1980s. By contrast, no significant differences between the periods of 2001–2010 and 1981–1990 are found in the first four PCs' variances of the WPISO.

To obtain further insight into the features of the IOISO and WPISO, composite life cycles of OLR and low-level circulation were compared (Figs. 6, 7). L13 showed the BSISO life cycle constructed by the BSISO EOF1 and EOF2 modes. The same method was applied to define 8

Fig. 6 **a** The life cycle composite (phases 1–8) of OLR (*shading*) and 850-hPa wind (*vector*) anomalies reconstructed based on the IOISO PC1 and PC2 [$(PC1^2 + PC2^2)^{1/2} > 1.50$]. **b** Number of occurrence for each phase with large amplitude during 1981–2010. Composite maps shown in (a) are masked to exhibit only anomalies that exceed a two tailed Normal- z test at the 95 % confidence level. The *purple rectangle* in (a) indicates the MV-EOF domain for the IOISO

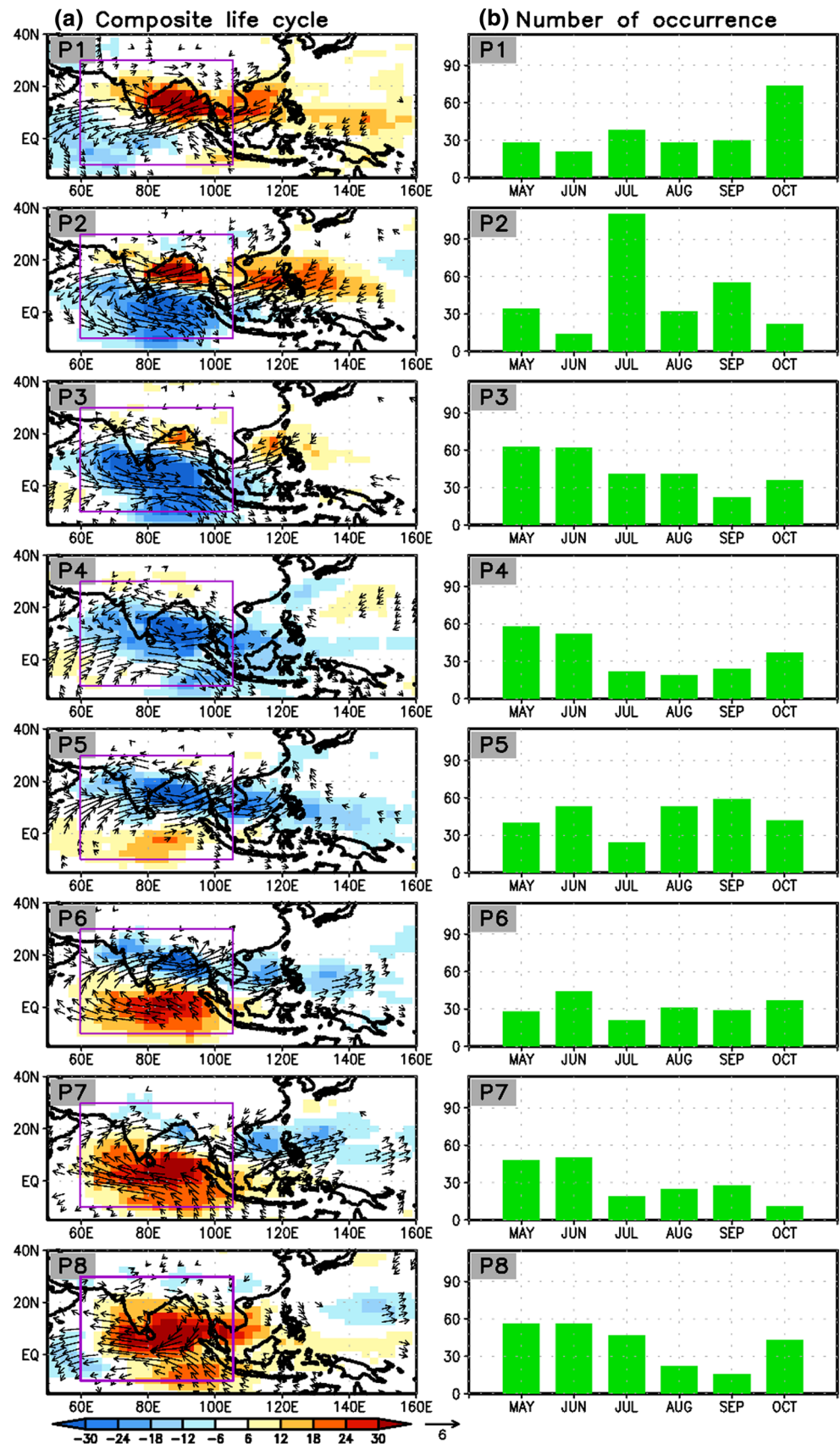
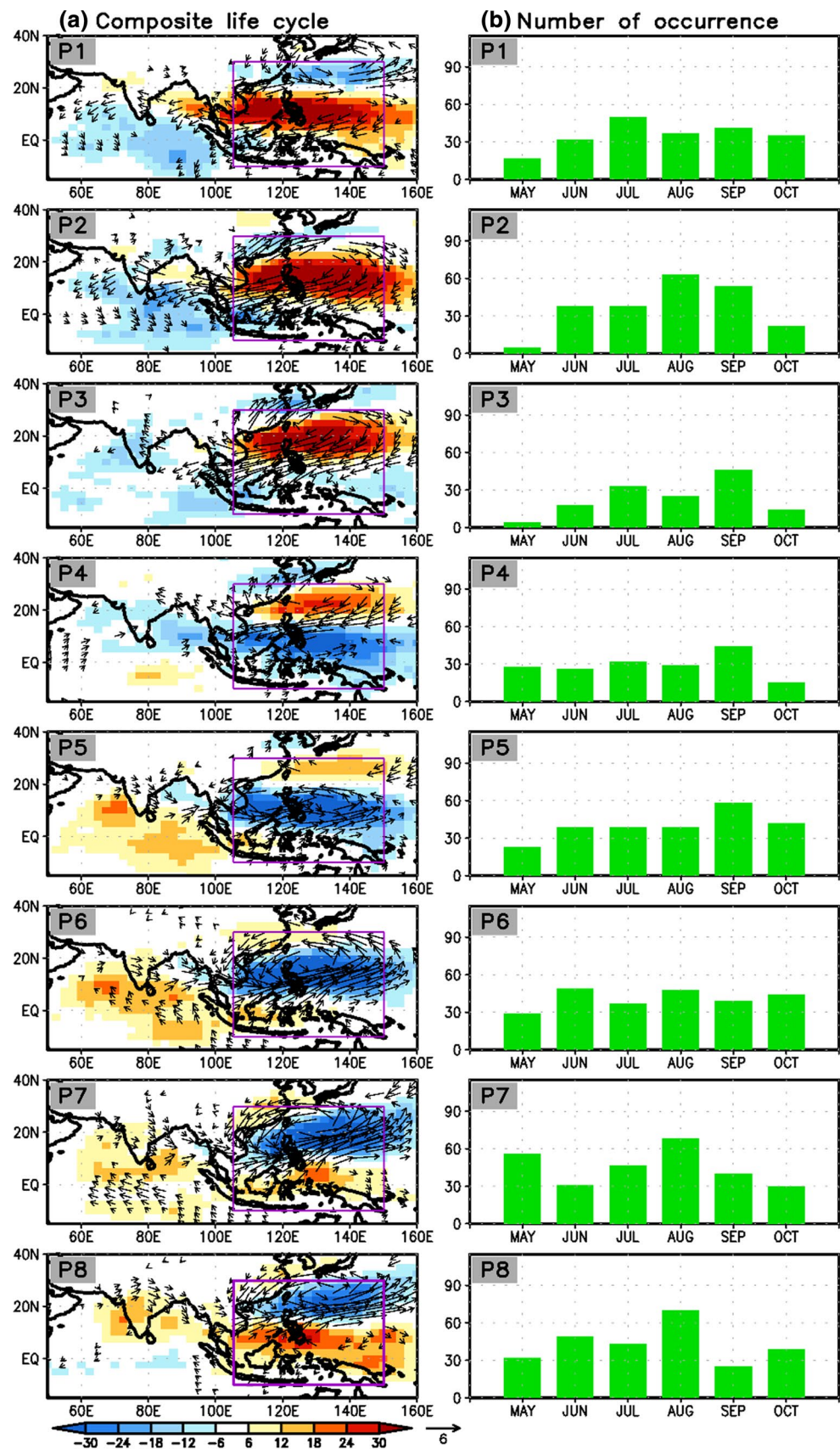


Fig. 7 Same as Fig. 6 except for the WPISO



phases of the IOISO (WPISO) and make its related composite fields based on the magnitudes and signs of the PC1 and PC2 of the IOISO (WPISO). The composite life cycles with large amplitude [$(PC1^2 + PC2^2)^{1/2} > 1.50$] were presented (Figs. 6a, 7a) and these composite life cycles may be simply called IOISO and WPISO life cycle, respectively. In addition, we explored the occurrence number of each phase to see whether the frequency of any phase's occurrence is distinctly higher or lower than that of other phases at a specific time.

The differences in life cycles between the IOISO (Fig. 6a) and WPISO (Fig. 7a) are found in the propagation direction. A convective anomaly associated with the IOISO commences in the equatorial Western IO at phase 1 and it propagates northeastward. The strong convection anomaly is found in the equatorial IO at phases 2 and 3. At phases 5 and 6, the convection anomaly reaches the Bay of Bengal and the NW–SE tilted convection anomaly is developed from the Bay of Bengal to Philippine Sea. These phases resemble the active phase documented by Suhas et al. (2013), which shows positive rainfall anomalies over the India landmass. The features of the IOISO's life cycle are similar to those of the BSISO shown in L13.

Figure 6b shows the occurrence number of 8 phases with large amplitudes [$(PC1^2 + PC2^2)^{1/2} > 1.50$] as a function of month. Overall, strong events related to the IOISO occur frequently in May and June, particularly for phases 3, 4, 7 and 8, which has monotonic convection anomaly in the IO. The high frequency of strong events in May and June may be related to the high variances of the IOISO PC1 and PC2 in corresponding months (Fig. 5a). Moreover, several phases show a noticeable seasonal preference for their occurrences. The strong events of phase 1 occur 74 cases in October, which is about 34 % of total strong cases of phase 1 (219 cases), but 21 cases occur in June, which is about 10 % of total strong events. For the strong events of phase 2, most of its occurrence is found in July, which accounts for about 41 %, but only about 5 % occurs in June. For phase 7, June is the most favorable (about 28 %) and October is the least favorable (about 6 %), which is opposite to that of phase 1. The occurrence difference between the most favorable and least favorable months is less than 20 % for other phases.

On the other hand, for the WPISO life cycle (Fig. 7a), anomalous convection center features a northward movement. The weak convection anomaly over the maritime continent at phases 1 and 2 is originated by eastward propagation of the ISO from the IO. The convective anomaly then migrates northward and is intensified, reaching the maximum over the WP at phases 5 and 6. Obviously, this northward propagation is dominated by 30–60 days oscillation because the biweekly component moves westward (Kikuchi and Wang 2009). The WP is one of sectors that

shows independent northward propagation of ISO (Wang and Rui 1990) and this is closely related to the decay of the equatorial ISO convective activity near the dateline and the impacts of the northern summer monsoon circulation and basic-state moist static energy distribution (Wang and Xie 1997). The composite WPISO fields exhibit more evident seesaw oscillation of convection between the IO and WP.

Unlike the IOISO, most phases' strong WPISO events show high frequency of occurrence in August and September and low frequency in May and June, except for the phase 7 (Fig. 7b). In particular, phases 2 and 3 of the WPISO exhibit a strong seasonal preference. For phase 2, May is the least favorable month (about 2 %) whereas August is the most favorable month (about 29 %). For phase 3, only about 3 % of strong cases occurs in May, but about 46 % of strong cases occurs in September. The seasonal preference of each phase and its possible reasons need further analysis.

4 Intrinsic ISO modes over the IO and WP in the ISVHE models

To assess models' intrinsic ISV features, we examined the simulated major modes of the IOISO and WPISO using available four (ECMWF, JMAC, CMCC, CFS2) models' free coupled run data. The procedures to obtain OLR and U850 anomalies and the leading ISO modes over the IO and WP are same as those adopted in observation, and 10 years (ECMWF) or 20 years (JMAC, CMCC, CFS2) data were analyzed.

Figure 8 shows the first two leading modes of the IOISO/WPISO derived from the ECMWF and CMCC as an example. In the ECMWF, the first two EOF modes of the IOISO and WPISO account for about 25 and 22 % of total combined daily variance of OLR and U850 over the individual region, respectively, and these values are comparable to the observation. The first two leading modes of other models show similar percent variance as the observation, which is about 22–25 %, except for the IOISO EOF1 and EOF2 in the JMAC (explain 17 % of total daily variance) (not shown). It is noted that the principal modes of the IOISO and WPISO are reasonably well simulated in the four models, but models have some shortcomings. For example, for the IOISO, the EOF1 in the ECMWF resembles more closely observed EOF2 mode (pattern correlation coefficient 'PCC' of OLR is 0.81) than observed EOF1 (PCC of OLR is -0.60). The PCC of OLR between the ECMWF EOF2 and observed EOF1 is 0.84. Meanwhile, for the WPISO, the PCC of OLR between the ECMWF and observation is 0.93 for the EOF1 and 0.87 for the EOF2, indicating that ECMWF can capture the spatial distributions related to the WPISO. However, the CMCC has difficulty in simulating the leading modes of the WPISO (PCC of

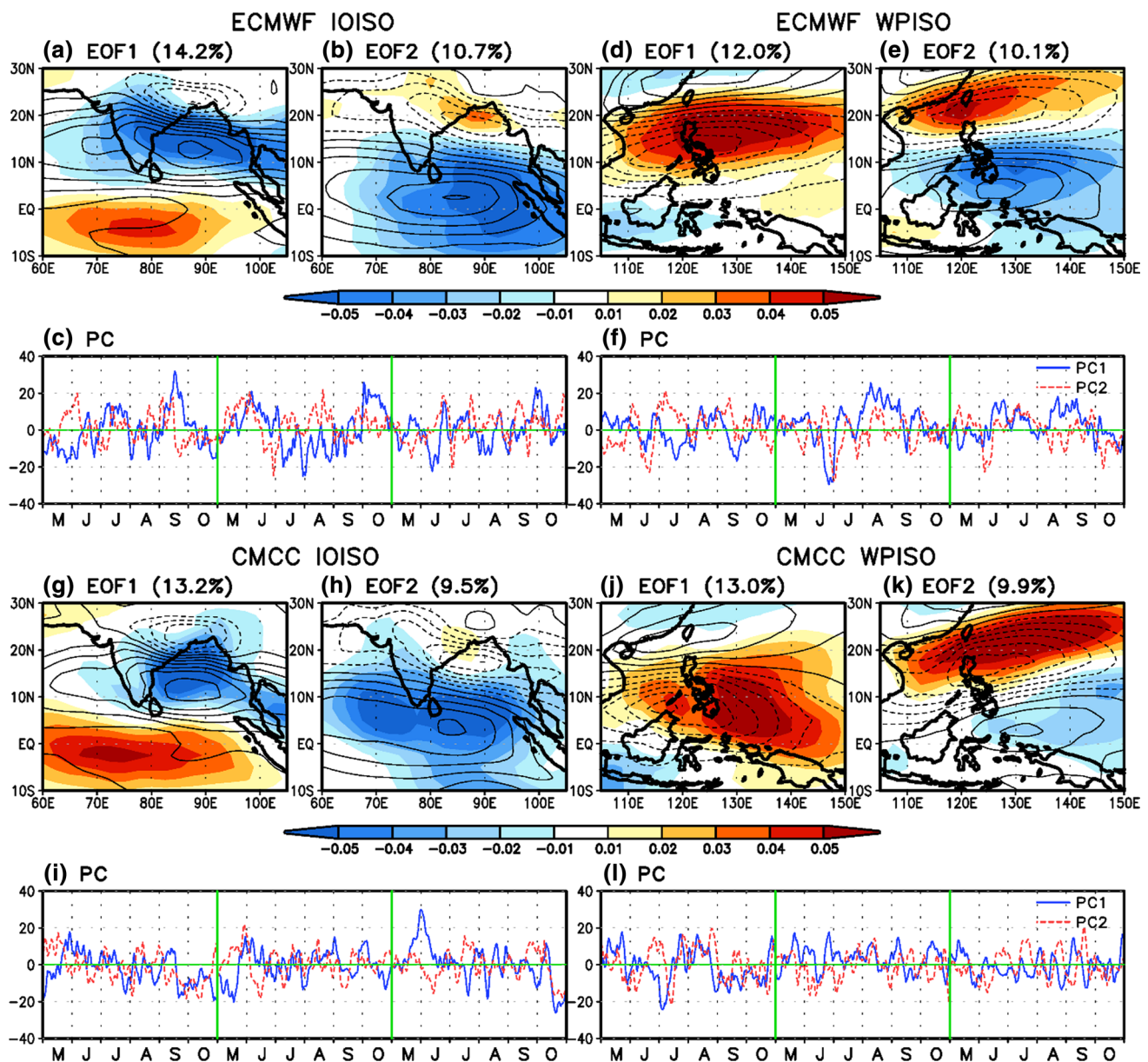


Fig. 8 **a, b** Spatial structures and **c** PC time series of the first two leading MV-EOF modes of daily OLR (*shading*) and 850-hPa zonal wind (U850) anomalies over the IO region (10°S–30°N, 60°–105°E) obtained from the ECMWF free run data (MJJASO for the 10 years). **d–f** Same as **a–c** except for the WP region (10°S–30°N, 105°–

150°E). **g–i** and **j–l** Same as (**a–c**) and (**d–f**), respectively, except for the CMCC free run data (MJJASO for the 20 years). To display the full *horizontal wind vector*, the associated 850-hPa meridional wind (V850) was obtained by regressing V850 anomaly against each PC

OLR is 0.45 for the EOF1 and 0.65 for the EOF2). Our results can help identify models' deficiencies and suggest ways to improve models' ability to represent the regional BSISO.

5 Predictability and prediction skill of the IOISO and WPISO

Using six models' hindcast data of ISVHE project, Lee et al. (2015) estimated the predictability and prediction

skill of the BSISO index. They showed that the multi-model mean predictability and prediction skill of the BSISO index with large initial amplitude are about 45 and 22 days, respectively. Similarly, in the present study, we examined the predictability and prediction skill of the IOISO and WPISO utilizing same hindcast data. To determine the predictability and prediction skill, we applied the 'ensemble-mean method' with the perfect model assumption (Neena et al. 2014b; Lee et al. 2015) using the IOISO and WPISO indices in the observation and hindcast. The

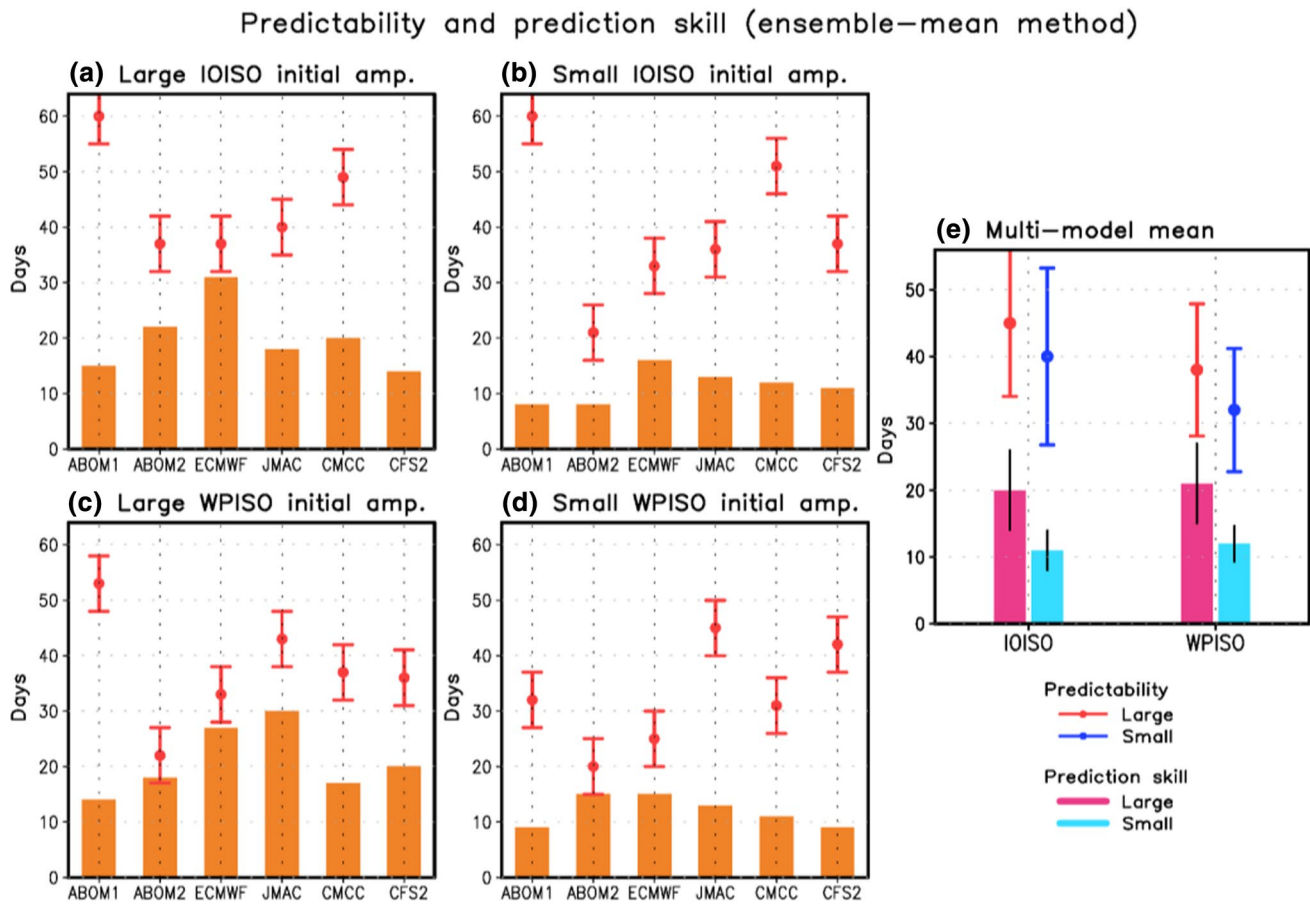


Fig. 9 The predictability (± 5 days range) and prediction skill of the IOISO and WPISO indices with **a, c** large initial amplitude and **b, d** small initial amplitude. **e** Multi-model mean predictability and pre-

diction skill for the IOISO and WPISO indices with large and small initial amplitudes. The *error bars* of predictability and prediction skill in **e** represent the 95 % confidence interval

hindcast IOISO (WPISO) index was obtained by projecting the two combined anomalous fields (OLR and U850) of hindcast onto the observed first two IOISO (WPISO) EOF modes.

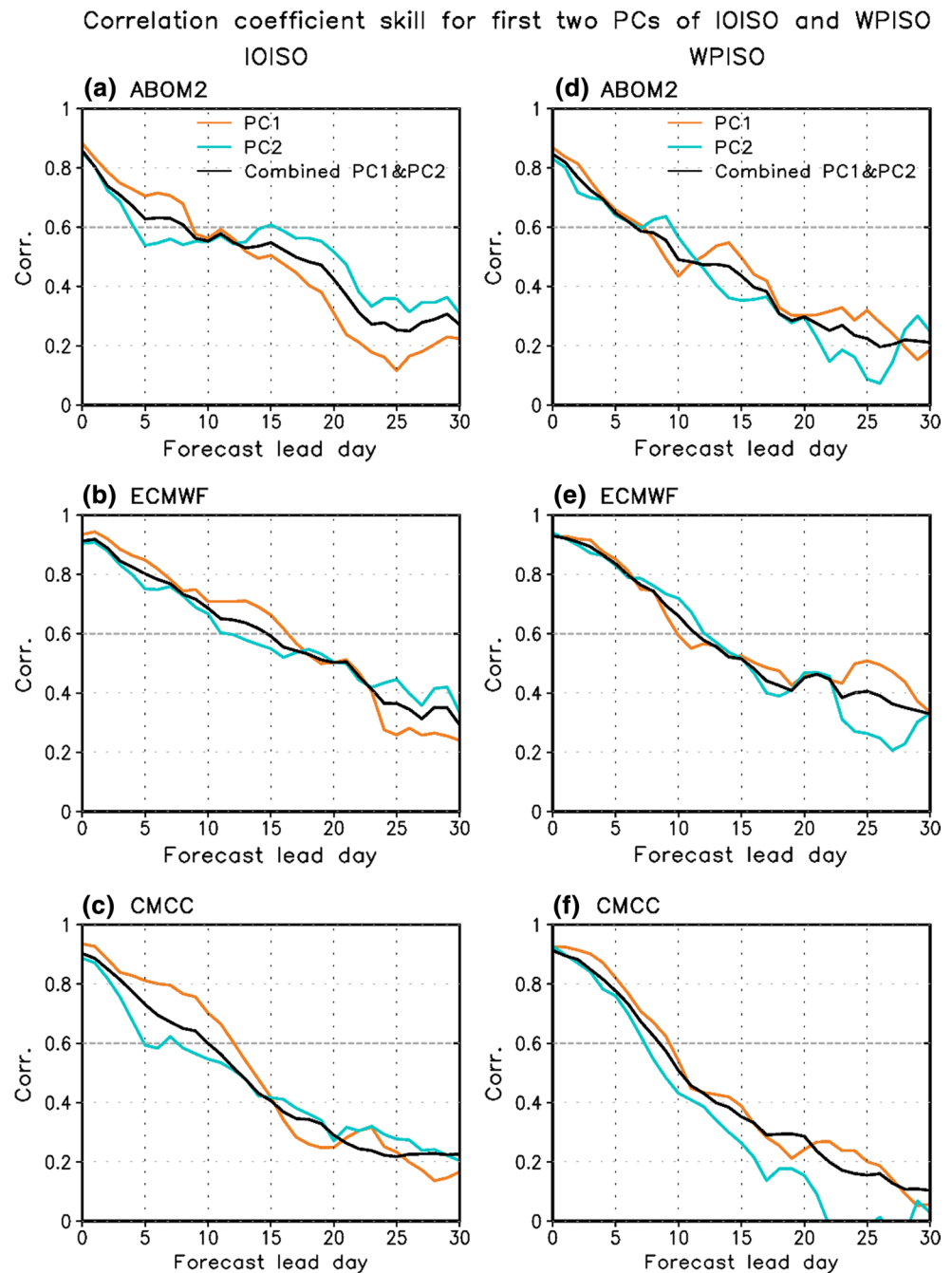
In the ensemble-mean approach for estimation of the predictability, the signal was obtained from the mean amplitude of hindcast IOISO/WPISO index (a single ensemble member designated as ‘control’) within a sliding window (sliding window is set to 51 day in the present study). The error growth was estimated by the difference between the single ensemble member (‘control’) and the ensemble mean of all other ensemble members that are designated as ‘perturbations’. For the prediction skill estimation, the signal was obtained from the observed IOISO/WPISO index (‘control’) and the forecast error was measured by the difference between the observation and the ensemble mean (averaged over all ensemble members) forecast (‘perturbation’). The predictability and prediction skill are defined as the forecast lead day when the signal and forecast error intersect. Details of equations and their explanations of the ensemble-mean

approach are given in Neena et al. (2014b) and Lee et al. (2015).

In order to evaluate the initial amplitude effect on the predictability and prediction skill, we divided the hindcast of individual model into two groups based on the observed initial amplitude. The strong and weak IOISO (WPISO) initial conditions are defined as the observed IOISO (WPISO) index’s amplitude at 0-day of the hindcast is greater than 1.50 [$(PC1^2 + PC2^2)^{1/2} > 1.50$] and less than 0.80 [$(PC1^2 + PC2^2)^{1/2} < 0.80$], respectively.

Figure 9 shows the resultant predictability and prediction skill estimates of the IOISO and WPISO indices using six climate models’ hindcast data. For the strong IOISO initial condition, in the CFS2, the signal and error do not intersect within its integrations days (44 days) (not shown), and thus the predictability in the CFS2 was not estimated. For the estimation of six models’ mean predictability, we assumed that the predictability in the CFS2 is 45 days. The multi-model mean predictability of the IOISO index with large IOISO initial amplitude is about 45 days (ranging from 37 to 60 days) and the corresponding predictability with small

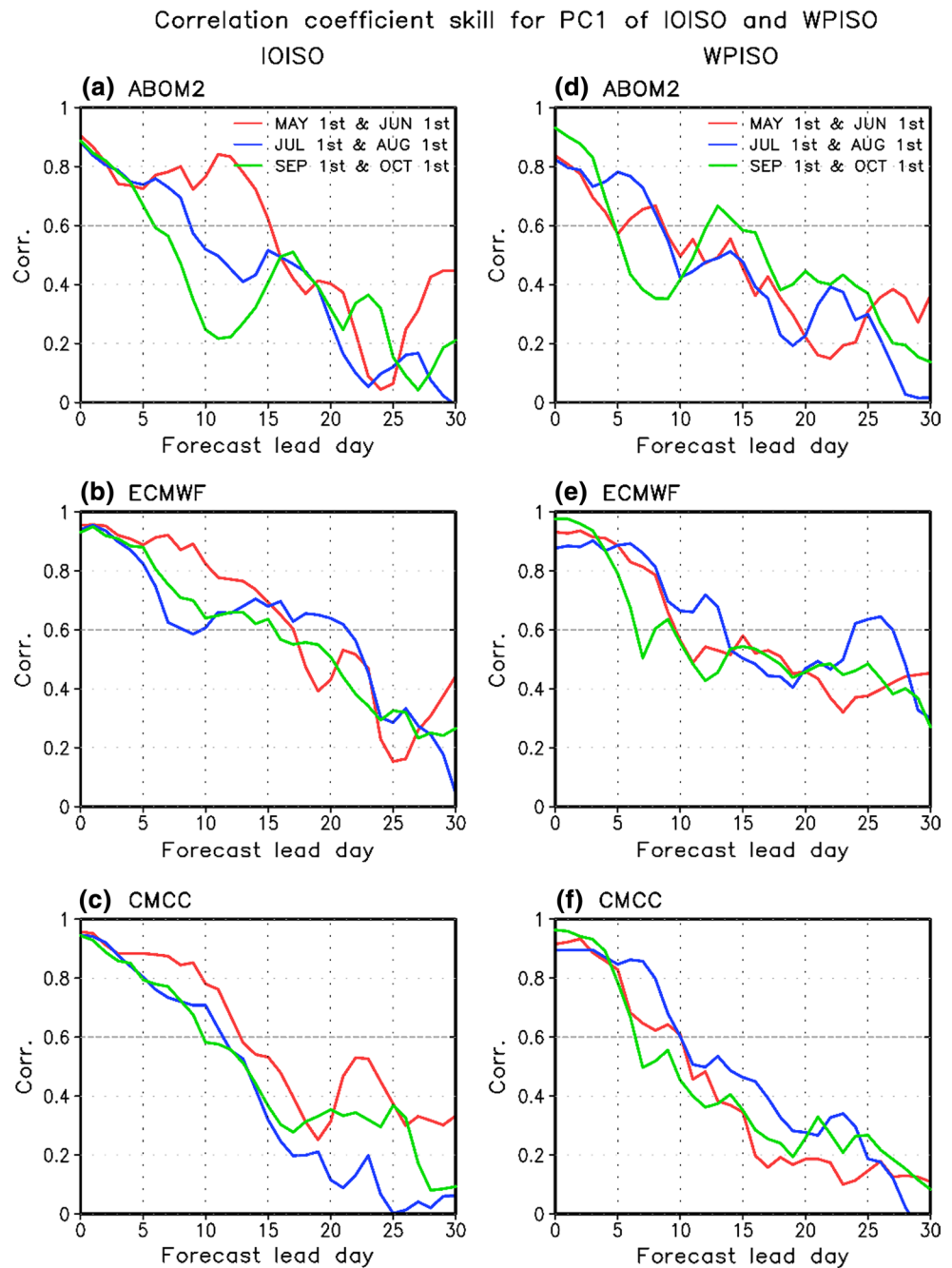
Fig. 10 Correlation coefficient skill for the first two PCs of the IOISO and WPISO with all summer initial conditions (May 1st, June 1st, ..., October 1st) in **a, d** ABOM2, **b, e** ECMWF, and **c, f** CMCC



IOISO initial amplitude is about 40 days (ranging from 21 to 60 days). These values are comparable with the BSISO predictability estimated by the BSISO index with same criteria for large and small initial amplitudes, which show about 44 days in both initial conditions (not shown). For the predictability of the WPISO index, the multi-model mean estimates are about 37 days in large WPISO initial amplitude and 33 days in small WPISO initial amplitude. It is noted that the predictability of the WPISO index is about 8 days lower than that of the IOISO index, indicating that the WPISO is less predictable than the IOISO. Fu et al.

(2007) suggested two reasons for the lower predictability of the WPISO. First, the ISO variability in this region may be underestimated. Second, the forecast errors tend to grow faster in the WP. Additionally, the less predictable WPISO could be partially due to the strong interannual variability of ISO over the WP (Teng and Wang 2003; Kim et al. 2008). We speculate that the lower predictability in the WP may be due to the existence of the biweekly component of the WPISO (Fig. 4c, d) which has shorter period. More work is needed to further understand the reasons for the lower predictability of WPISO. When we consider

Fig. 11 Correlation coefficient skill for the PC1 of the IOISO and WPISO with different initial conditions in **a, d** ABOM2, **b, e** ECMWF, and **c, f** CMCC. Red, blue, green curves indicate the correlation coefficient of the PC1 between observation and models with 'May 1st and June 1st', 'July 1st and August 1st', and 'September 1st and October 1st' initial conditions, respectively



the multi-model mean estimates, result of Fig. 9e reveals that there is no significant difference of the predictability between large and small initial amplitudes for both the IOISO and WPISO.

From a prediction skill perspective, comparing Fig. 9a, c with Fig. 9b, d indicates that the prediction skill with large initial amplitude is always higher than corresponding skill with small initial amplitude in all six models. Figure 9e shows that the multi-model mean prediction skill of the IOISO index with large IOISO initial amplitude is about 20 days and this is significantly higher than corresponding

skill with the small IOISO initial amplitude, which is about 11 days. For the WPISO index, the multi-model mean prediction skills are estimated about 21 days with large WPISO initial amplitude and 12 days with small WPISO initial amplitude. The significant difference of prediction skills between large and small initial amplitudes indicates that the prediction for development process of the regional BSISO is much more difficult than the prediction for mature BSISO disturbances' propagation. It also supports the notion that improved initial condition is important for ISO prediction skills (Fu et al. 2009, 2011; Lee et al. 2015).

Furthermore, we examined the dependency of prediction skill on the initial season by comparing the correlation coefficients of ensemble mean with observation. Three models (ABOM2, ECMWF, CMCC) that are initialized from the 1st day of every month for 19–20 year hindcast period were selected for this comparison. The prediction skill is estimated by the forecast lead day when the correlation dropped below a threshold of 0.6 (Suhas et al. 2013). If all summer initial conditions (from May to October) are considered, three models' prediction skills are around 9–17 days for the IOISO PC1 and 8–10 days for the WPISO PC1 (Fig. 10). The ECMWF exhibits the best skill for both the IOISO PC1 and WPISO PC1. Suhas et al. (2013) showed that the prediction skills of their monsoon ISO index 1 and 2 are about 13 and 9 days, respectively. The bivariate correlation skills obtained from both the PC1 and PC2 (Lin et al. 2008) are 8–14 days for the IOISO and 7–11 days for the WPISO.

When we consider the different initial season, it is found that the correlation skills of the IOISO and WPISO vary considerably with the initial season (Fig. 11). Interestingly, all three models show the best skills for the IOISO PC1 with May 1st and June 1st initial conditions, and this may be related to the high variance of the IOISO PC1 in early summer (Fig. 5a). For the WPISO, two models tend to show higher skills with July 1st and August 1st initial conditions and lower skills when it is initiated from September 1st and October 1st. This result indicates that the prediction skills of the IOISO and WPISO tend to be dependent on the initial season and it might be associated with its season-dependent variance distribution.

6 Summary

The purpose of this study is to compare the regional BSISO features over the IO and WP based on the identical metrics and to estimate their predictability and prediction skill in the current climate models. An important motivation is to see whether the regional ISO modes can capture a more significant portion of total variance over the targeted region than the BSISO's leading modes, so that the prediction of regional ISO may improve sub-seasonal prediction.

The MV-EOF analysis was applied using daily OLR and U850 anomalies for boreal summer over the regions of [10°S–30°N, 60°–105°E] and [10°S–30°N, 105°–150°E], respectively, in order to obtain the major spatial–temporal structures of the IOISO and WPISO. To better represent the fractional variance over the ASM region (10°S–40°N, 40°–160°E), we considered the combined ISO modes derived from the first two PCs of the IOISO and WPISO. The individual daily variance of OLR and U850 over the ASM region can be better explained by the combined

IOISO–WPISO index compared with the MJO (RMM) index and BSISO index (Fig. 2). In particular, the combined IOISO–WPISO index captures about 10 % for OLR and 30 % for U850 daily variance over the IO–WP region (10°S–30°N, 60°–150°E), and these values double those captured by the MJO (RMM) index and are 50 % higher than those captured by the BSISO index. It is noteworthy that the combined index is very useful to represent the biweekly and ISO variances in the regions north of 10°N.

From the comparison of the leading modes of the IOISO and WPISO, it is noted that the IOISO and WPISO distinguish from each other by the periodicity (30–45 days periodicity vs. multi-time scale variability of 10–60 days) (Fig. 4), seasonal distribution of the PCs' variances (PC1 peak in May, double peaks of PC2 and PC3 in May–June and October–November vs. PC1 peak in August) (Fig. 5a), and propagating features (northeastward vs. northward) (Figs. 6a, 7a). In particular, the IOISO PC1 variance in May and August shows the significant interdecadal trend, indicating that in May and August the strong enhanced convection over the equatorial IO with suppressed convection over the Bay of Bengal (and vice versa) occurs frequently during recent years (the period of 2001–2010) compared with the 1980s. Moreover, we found that several phases of the IOISO and WPISO have the distinct seasonal preference of their occurrences. These results may have important implications for mining predictability sources of the IOISO and WPISO.

By analysis of two experimental datasets of the ISVHE project, current models' ability to represent the regional BSISO variability was explored. The principal modes of the IOISO and WPISO are reasonably well simulated, but models have shortcomings in presenting detailed spatial structures of regional BSISO (Fig. 8). From the predictability perspective, the multi-model mean estimate of the IOISO index is about 40–45 days for both large and small initial amplitudes, and this is about 8 days higher than the predictability of the WPISO index (33–37 days) (Fig. 9). The less predictable WPISO is likely due to its significant biweekly component. Comparison of the predictability between large and small initial amplitudes confirms that the initial amplitude does not significantly affect the estimation of predictability of the IOISO/WPISO, similar to the BSISO (Lee et al. 2015).

Different from the predictability, the initial amplitude and initial season may play a role in determining the prediction capability of the IOISO and WPISO (Figs. 9, 11), indicating that prediction for the development process of the regional BSISO is difficult and improvement of initial condition is important for the success of ISO's predictions (Fu et al. 2009, 2011; Lee et al. 2015). Current levels of prediction skills for the IOISO and WPISO indices with large initial amplitude are around 20 days and these

are 9 days higher compared with corresponding skills with small initial amplitude. The prediction skills of the IOISO and WPISO with large initial amplitude are comparable with corresponding skill of the MJO index (Neena et al. 2014b) and higher than the Eastern Pacific ISO prediction skill which shows 10–14 days (Neena et al. 2014a). Finally, it is noted that there is still wide discrepancy of the prediction skill as well as the predictability estimates between current climate models. This deserves future studies for developing optimal strategy of multi-model ensemble.

Acknowledgments This work was jointly supported by the NOAA/MAPP project Award number NA10OAR4310247, APEC climate center (APCC), and the National Research Foundation (NRF) of Korea through a Global Research Laboratory (GRL) grant of the Korean Ministry of Education, Science and Technology (MEST, #2011-0021927). BW acknowledges support from NOAA/ESS program, under Project NA13OAR4310167. This is publication No. 9433 of the SOEST, publication No. 1123 of IPRC, and publication No. 052 of Earth System Modeling Center (ESMC).

References

- Bellenger H, Duvel JP (2007) Intraseasonal convective perturbations related to the seasonal march of the Indo-Pacific monsoons. *J Clim* 20:2853–2863
- Chou C, Hsueh Y (2010) Mechanisms of northward-propagating intraseasonal oscillation—a comparison between the Indian Ocean and the western north Pacific. *J Clim* 23:6624–6640
- Fu X, Wang B, Waliser D, Tao L (2007) Impact of atmosphere–ocean coupling on the predictability of monsoon intraseasonal oscillations. *J Atmos Sci* 64:157–174
- Fu X, Wang B, Bao Q, Liu P, Lee JY (2009) Impacts of initial conditions on monsoon intraseasonal forecasting. *Geophys Res Lett* 36:L08801. doi:10.1029/2009GL037166
- Fu X, Wang B, Lee JY, Wang W, Gao L (2011) Sensitivity of dynamical intraseasonal prediction skills to different initial conditions. *Mon Wea Rev* 139:2572–2592
- Goswami BN, Ajayamohan RS, Xavier PK, Sengupta D (2003) Clustering of synoptic activity by Indian summer monsoon intraseasonal oscillations. *Geophys Res Lett* 30:1431
- Jiang X, Li T, Wang B (2004) Structures and mechanisms of the northward-propagating boreal summer intraseasonal oscillation. *J Clim* 17:1022–1039
- Kanamitsu M et al (2002) NCEP dynamical seasonal forecast system 2000. *Bull Am Meteorol Soc* 83:1019–1037
- Kemball-Cook S, Wang B (2001) Equatorial waves and air–sea interaction in the boreal summer intraseasonal oscillation. *J Clim* 14:2923–2942
- Kikuchi K, Wang B (2009) Global perspectives of the quasi-biweekly oscillation. *J Clim* 22:1340–1359
- Kim HM, Kang IS (2008) The impact of ocean–atmosphere coupling on the predictability of boreal summer intraseasonal oscillation. *Clim Dyn* 31:859–870
- Kim HM, Kang IS, Wang B, Lee JY (2008) Interannual variations of the boreal summer intraseasonal variability predicted by ten atmosphere–ocean coupled models. *Clim Dyn* 30:485–496
- Krishnamurthy V, Shukla J (2008) Seasonal persistence and propagation of intraseasonal patterns over the Indian monsoon region. *Clim Dyn* 30:353–369
- Lawrence D, Webster PJ (2002) The boreal summer intraseasonal oscillation and the South Asian monsoon. *J Atmos Sci* 59:1593–1606
- Lee JY, Wang B, Wheeler M, Fu X, Waliser D, Kang IS (2013) Real-time multivariate indices for the boreal summer intraseasonal oscillation over the Asian summer monsoon region. *Clim Dyn* 40:493–509
- Lee SS, Wang B, Waliser D, Neena JM, Lee JY (2015) Predictability and prediction skill of the boreal summer intraseasonal oscillation in the Intraseasonal Variability Hindcast Experiment. *Clim Dyn*. doi:10.1007/s00382-014-2461-5 **published online**
- Liebmann B, Smith CA (1996) Description of a complete (interpolated) outgoing longwave radiation dataset. *Bull Am Meteor Soc* 77:1275–1277
- Liebmann B, Hendon H, Glick J (1994) The relationship between tropical cyclones of the western Pacific and Indian Oceans and the Madden–Julian Oscillation. *J Meteor Soc Jpn* 72:401–412
- Lin H, Brunet G, Derome J (2008) Forecast skill of the Madden–Julian Oscillation in two Canadian atmospheric models. *Mon Wea Rev* 136:4130–4149
- Maloney E, Hartmann D (2001) The Madden–Julian Oscillation, barotropic dynamics, and North Pacific tropical cyclone formation. Part I: observations. *J Atmos Sci* 58:2545–2558
- Moon JY, Wang B, Ha KJ, Lee JY (2013) Teleconnections associated with Northern Hemisphere summer monsoon intraseasonal oscillation. *Clim Dyn* 40:2761–2774
- Neena JM, Jiang X, Waliser D, Lee JY, Wang B (2014a) Eastern Pacific Intraseasonal Variability: a predictability perspective. *J Clim* 27:8869–8883
- Neena JM, Lee JY, Waliser D, Wang B, Jiang X (2014b) Predictability of the Madden–Julian Oscillation in the Intraseasonal Variability Hindcast Experiment (ISVHE). *J Clim* 27:4531–4543
- Pegion K, Kirtman BP (2008) The impact of air–sea interactions on the predictability of the tropical intraseasonal oscillation. *J Clim* 21:5870–5886
- Sengupta D, Senan R, Goswami BN (2001) Origin of intraseasonal variability of circulation in the tropical central Indian Ocean. *Geophys Res Lett* 28:1267–1270
- Shukla RP (2014) The dominant intraseasonal mode of intraseasonal South Asian summer monsoon. *J Geophys Res* 119:635–651
- Suhas E, Neena JM, Goswami BN (2013) An Indian monsoon intraseasonal oscillation (MISO) index for real time monitoring and forecast verification. *Clim Dyn* 40:2605–2616
- Teng H, Wang B (2003) Interannual variations of the boreal summer intraseasonal oscillation in the Asian-Pacific region. *J Clim* 16:3572–3584
- Waliser D, Jin K, Kang IS, Stern WF et al (2003) AGCM simulations of intraseasonal variability associated with the Asian summer monsoon. *Clim Dyn* 21:423–446
- Wang B (1992) The vertical structure and development of the ENSO anomaly mode during 1979–1989. *J Atmos Sci* 49:698–712
- Wang B, Rui H (1990) Synoptic climatology of transient tropical intraseasonal convection anomalies. *Meteor Atmos Phys* 44:43–61
- Wang B, Xie X (1996) Low-frequency equatorial waves in vertically shear flow. Part I: stable waves. *J Atmos Sci* 53:449–467
- Wang B, Xie X (1997) A model for the boreal summer intraseasonal oscillation. *J Atmos Sci* 54:72–86
- Wheeler M, Hendon HH (2004) An all-season real-time multivariate MJO index: development of an index for monitoring and prediction. *Mon Wea Rev* 132:1917–1932
- Yim SY, Wang B, Liu J, Wu Z (2014) A comparison of regional monsoon variability using monsoon indices. *Clim Dyn* 43:1423–1437
- Zhang C, Gottschalck J, Maloney ED, Moncrieff MW, Vitart F, Waliser D, Wang B, Wheeler MC (2013) Cracking the MJO nut. *Geophys Res Lett* 40:1223–1230
- Zhu B, Wang B (1993) The 30–60 day convection seesaw between the tropical Indian and western Pacific Oceans. *J Atmos Sci* 50:184–199